

Bridging Physically Based Rendering and Diffusion Models with Stochastic Differential Equation

Junwei Shu^{1,*} Wenjie Liu^{1,*} Changgu Chen¹ Hantang Liu² Yang Li^{1,†} Changbo Wang^{3,†}

¹School of Computer Science and Technology, East China Normal University

²Kun Byte, ³School of Data Science and Engineering, East China Normal University

Abstract

Diffusion-based image generators excel at producing realistic content from text or image conditions, but they offer only limited explicit control over low-level, physically grounded shading and material properties. In contrast, physically based rendering (PBR) offers fine-grained physical control but lacks prompt-driven flexibility. Although these two paradigms originate from distinct communities, both share a common evolution—from noisy observations to clean images. In this paper, we propose a unified stochastic formulation that bridges Monte Carlo rendering and diffusion-based generative modeling. First, a general stochastic differential equation (SDE) formulation for Monte Carlo integration under the Central Limit Theorem is modeled. Through instantiation via physically based path tracing, we convert it into a physically grounded SDE representation. Moreover, we provide a systematic analysis of how the physical characteristics of path tracing can be extended to existing diffusion models from the perspective of noise variance. Extensive experiments across multiple tasks show that our method can exert physically grounded control over diffusion-generated results, covering tasks such as rendering and material editing.

1. Introduction

In recent years, diffusion-based generative models [25–27, 30, 35] have achieved remarkable success in high-fidelity image synthesis, excelling at generating realistic and diverse images from text prompts or other conditions [50]. These models typically learn to approximate the data distribution via a stochastic denoising process, gradually transforming Gaussian noise into structured visual content through a reverse-time stochastic differential equation (SDE). Despite their empirical success, diffusion models remain largely empirical in nature: the denoising dynamics



Figure 1. Monte Carlo Sampling Based Rendering (first row) vs. Denoising Models (second row). These two methods share a similar formulation: involving a process with noise decreasing from high to low.

are data-driven, the latent representations lack physical interpretability, and the entire process is detached from the physical principles of image formation.

In contrast, physically based rendering (PBR) [7] provides a principled foundation for realistic image generation grounded in light transport physics. Monte Carlo path tracing [13], a widely used approach in PBR, computes the rendering equation via stochastic sampling. The rendered image gradually converges from a noisy estimator to a clean, converged result as the number of samples increases. Interestingly, this refinement process, which starts from stochastic noise and converges to a clean image, is analogous to the evolution of diffusion-based denoising models (see Fig. 1). This observation naturally raises a fundamental question:

Can physically based rendering and diffusion-based generation be interpreted as two instances of a unified stochastic process?

In this paper, we answer this question by formulating Monte Carlo rendering and diffusion-based modeling within a unified stochastic framework. Firstly, we introduce the Monte Carlo stochastic differential equation (MC-SDE), which converts Monte Carlo integration into an SDE formulation, and then bridge the physical properties of PBR into

*Equal contribution.

†Corresponding author.

this framework. Specifically, we start from the Monte Carlo estimator and, under the Central Limit Theorem, derive its continuous-time limit as an SDE. This result reveals that any unbiased Monte Carlo estimator with finite variance can be expressed as a diffusion-like process. Such a formulation provides a mathematically rigorous connection between statistical sampling and generative diffusion processes. We then instantiate this general SDE within physically based path tracing, thereby enabling a physically grounded interpretation of the model.

Based on the physically grounded MC-SDE, we systematically analyze how the physical properties of PBR can be extended to existing diffusion models from the perspective of noise variance. Firstly, by matching the marginal variance for (variance exploding) VE [34] models and the signal-to-noise ratio (SNR) or standard deviation for VP/DDPM [11, 34] models, we derive a closed-form mapping between Monte Carlo “variance time” and the diffusion “timestep”. This conversion provides a physically meaningful initialization point when employing a diffusion model as a renderer. Moreover, physically based rendering (PBR) exhibits a characteristic disparity in variance, where the specular component shows significantly higher variance than the diffuse component. We analyze how this property manifests in the diffusion denoising process through an SNR framework. Specifically, the specular characteristics in the diffusion denoising process converge at relatively late stages, providing greater flexibility for adjustments throughout the entire denoising trajectory. This observation can be leveraged to achieve precise control over material appearance during the denoising process.

To validate the correctness of each aforementioned conclusion and its corresponding application, we design targeted experiments from the perspectives of rendering and material editing. The comprehensive results demonstrate that our method enables effective physical control over the outputs generated by existing diffusion models. In summary, our key contributions are threefold:

- We are the first to investigate the relationship between PBR and diffusion models from the perspective of their analogous denoising processes. To this end, a physically grounded MC-SDE is proposed, which serves as a bridge between PBR and diffusion models with SDE.
- Building on the physically grounded MC-SDE, we extend the physical properties of PBR to existing diffusion models by analyzing the behavior of noise variance.
- Extensive experimental results demonstrate that our method enables effective physical control over the outputs produced by existing diffusion models, including both rendering and material editing tasks.

2. Related Work

Diffusion Models for 2D Image Generation. Diffusion models excel at generating high-quality images by sampling from a learned distribution (e.g., photographs) [14, 34], particularly when conditioned on text prompts [25–27, 30]. Subsequent work has enhanced text-driven diffusion models to achieve higher-level semantic control over image generation [1, 2, 8, 9, 20, 23, 36, 39], including non-rigid semantic edits [4, 15], modifications to subject identity and gender [16], capture of underrepresented attribute distributions [6], and material property control [32]. However, except for Alchemist [32], these methods primarily offer mid- and high-level semantic control. Similar to Alchemist, our method targets low-level shading properties. While Alchemist provides relative control over material properties such as translucency and gloss, our approach enables fine-grained control over incident lighting in generated images.

Other guidance mechanisms have been introduced for spatial control during synthesis, using inputs such as sketch, depth, or stroke images [22, 38, 44], identity information [21, 29, 42], photo-collections [28], or direct manipulation of mid-level information [10, 24, 49]. However, none of these methods control incident lighting. Inspired by these approaches, we inject radiance hints—modulated by a neural encoded image representation—into the diffusion model via a ControlNet [49].

Diffusion Models with 3D. 2D diffusion models have been applied to alter viewpoints or generate 3D models [19, 40, 41, 48]. However, these methods neither control incident lighting nor ensure consistent lighting across viewpoints. Paint3D [46] directly generates diffuse albedo textures in the UV domain of a given mesh. Fantasia3D [5] and MatLaber [43] produce richer reflectance properties, such as shape and spatially-varying BRDFs, by leveraging text-to-image diffusion models and score distillation. Diffusion-based SVBRDF estimation [31, 37] and intrinsic decomposition [17] also generate reflectance properties, albeit from photographs rather than text prompts. However, all these methods require a rendering algorithm to visualize appearance, including indirect lighting and shadows. In contrast, our method is grounded in the commonality between path tracing and denoising models. Based on this foundation, we define materials for generated objects and their harmony with the background, leveraging the plausible image appearance and environment lighting embedded in diffusion models.

Furthermore, several works integrate diffusion models with traditional rendering concepts. For instance, environment maps are incorporated into diffusion models by some methods [12, 45], allowing objects to receive environmental lighting to some extent. Other works [18, 47] connect diffusion models with G-buffers, offering new perspectives

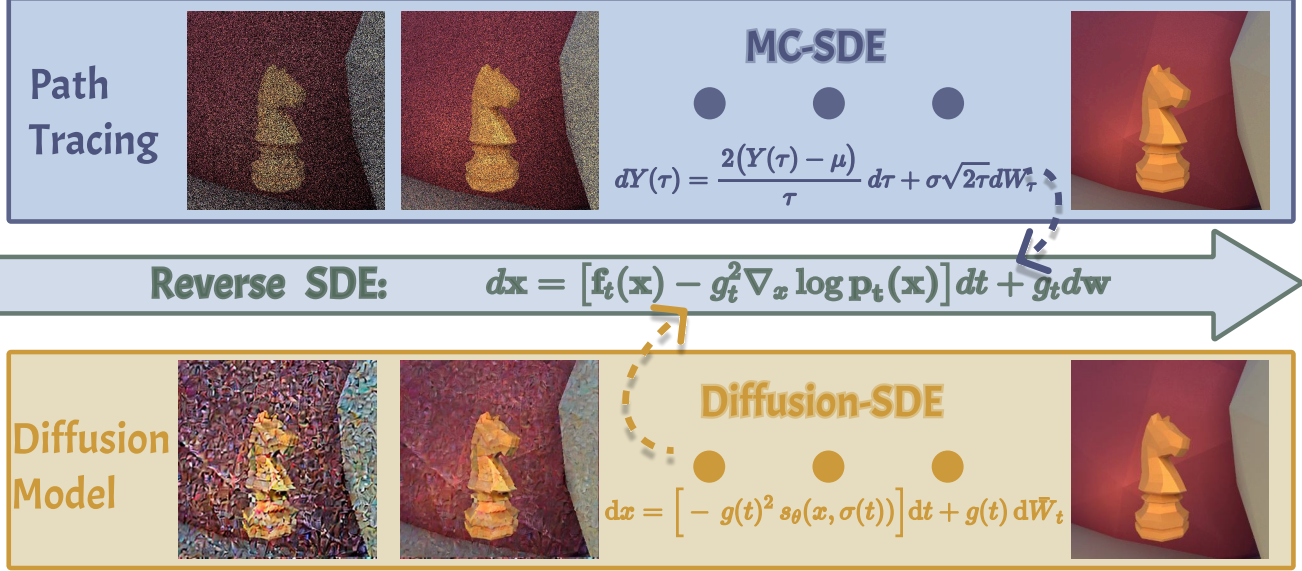


Figure 2. **MC-SDE ↔ Diffusion-SDE: variance-time alignment and unified noise.** **Top (Path Tracing).** Monte Carlo estimation is cast as a continuous process $Y(\tau)$ indexed by the *variance time* τ (large τ : few samples, high variance; $\tau \downarrow 0$: noise-free), contracting toward the mean radiance μ . **Middle (Reverse SDE).** The evolution matches the reverse dynamics of a clean-start VE process with noise scale $g(\tau)$; this provides a principled alignment between τ and diffusion-model time t by matching variance/SNR. **Bottom (Diffusion Model).** Using the $\tau \leftrightarrow t$ mapping, a pretrained diffusion model is sampled along the matched schedule $g(t)$; we instantiate path tracing with a *unified* noise source (shared random draws for diffuse/specular), so high-variance specular content dominates early denoising and the process converges to a clean image. *Summary.* We map τ to t via variance/SNR matching, with $\sigma(t) \propto \tau$ and $\text{SNR} \propto 1/\tau^2$, establishing the correspondence $g(\tau) \leftrightarrow g(t)$ and enabling physically interpretable schedules.

for forward and inverse rendering. However, to date, no work has addressed or formulated the commonality between these two approaches, which remains unexplored. This gap motivates our proposed stochastic formulation, bridging the diffusion model and path tracing into a unified stochastic process.

3. Methodology

This section we first formulate out the universal SDE of an MC-SDE. Then, the path tracing SDE based on MC-SDE is proposed. Finally, we bridge the SDE and diffusion models, scaling their noise level and conduct out the *specular domination* along these stochastic processes.

3.1. The SDE of Monte Carlo Integration

Monte Carlo estimators approximate an expected integration through repeated stochastic sampling. While this process is inherently discrete, its asymptotic behavior under the Central Limit Theorem (CLT) can be equivalently expressed as a continuous stochastic process. In this section, we derive a continuous-time SDE that governs the evolution of Monte Carlo estimators, providing a bridge between statistical sampling and diffusion-based denoising dynamics.

Discrete estimator. Consider a Monte Carlo estimator constructed from N independent and identically distributed

random samples F_k , drawn from an integrable distribution with mean μ and variance σ^2 :

$$X_N = \frac{1}{N} \sum_{k=1}^N F_k, \quad \mathbb{E}[F_k] = \mu, \quad \text{Var}(F_k) = \sigma^2. \quad (1)$$

According to the CLT, the estimator converges to a Gaussian distribution as N grows:

$$X_N \approx \mu + \frac{\sigma}{\sqrt{N}} \xi, \quad \xi \sim \mathcal{N}(0, 1). \quad (2)$$

This expression characterizes the noise statistics of Monte Carlo integration and forms the foundation for a continuous formulation. To align with the differential formulation of SDE, we next convert this expression into its continuous formulation.

Continuous formulation. To describe the sampling process in continuous time, we introduce a smooth, monotonic mapping between the discrete sample count N and a continuous variable $\tau > 0$:

$$N = N(\tau), \quad \text{with } \tau \rightarrow 0 \Rightarrow N(\tau) \rightarrow \infty. \quad (3)$$

We define the corresponding continuous process $Y(\tau)$ as

$$Y(\tau) := X_{N(\tau)}. \quad (4)$$

Intuitively, τ can be viewed as a “variance time”, with a large τ corresponding to few samples (high variance), and $\tau \rightarrow 0$ approaching infinite samples (variance-free).

Incremental update and differential. Consider a small time increment from τ to $\tau + \Delta\tau$. Let $\Delta N = N(\tau + \Delta\tau) - N(\tau) \approx N'(\tau) \Delta\tau$. The update of the estimator is given by

$$\begin{aligned} \Delta Y(\tau) &= X_{N+\Delta N} - X_N \\ &= -\frac{\Delta N}{N + \Delta N} X_N + \frac{1}{N + \Delta N} \sum_{k=N+1}^{N+\Delta N} F_k. \end{aligned} \quad (5)$$

Approximating $N + \Delta N \approx N$ and applying the local CLT for the new samples, we have

$$\sum_{k=N+1}^{N+\Delta N} F_k \approx \mu \Delta N + \sigma \sqrt{|\Delta N|} \xi, \quad \xi \sim \mathcal{N}(0, 1). \quad (6)$$

Substituting this expression yields

$$\Delta Y(\tau) \approx -\frac{N'(\tau)}{N(\tau)} Y(\tau) \Delta\tau + \frac{\mu N'(\tau)}{N(\tau)} \Delta\tau + \sigma \frac{\sqrt{|N'(\tau)|}}{N(\tau)} \sqrt{\Delta\tau} \xi. \quad (7)$$

Taking the limit $\Delta\tau \rightarrow 0$ and letting W_τ denote a standard Wiener process, we obtain the continuous-time SDE corresponding to the Monte Carlo averaging dynamics:

$$dY(\tau) = (\mu - Y(\tau)) \frac{N'(\tau)}{N(\tau)} d\tau + \sigma \frac{\sqrt{|N'(\tau)|}}{N(\tau)} dW_\tau. \quad (8)$$

This formulation replaces discrete sampling with a continuous diffusion process, whose drift and diffusion terms encode the estimator’s bias and variance evolution, respectively.

Noise Schedules. By writing out MC-SDE we can observe the same math modeling with diffusion model SDEs. Considering a standard diffusion Reverse SDE [34], corresponding to the denoising process:

$$d\mathbf{x} = [\mathbf{f}_t(\mathbf{x}) - g_t^2 \nabla_x \log \mathbf{p}_t(\mathbf{x})] dt + g_t d\mathbf{w}, \quad (9)$$

$\mathbf{f}_t(\mathbf{x})$ is the forward adding noise process drift term, $\mathbf{p}_t(\mathbf{x})$ is the distribution of data at time t , and g_t is the diffusion term, a.k.a. the noise schedule. A noise schedule is usually simple and monotone, indicating the noise scale at a certain timestep. And for a clean image ($t \rightarrow 0$), the noise scale is usually extremely small or just zero.

To ensure that the process approaches a noise-free state as $\tau \rightarrow 0$, like the diffusion model Reverse SDE, the diffusion term must vanish:

$$\lim_{\tau \rightarrow 0} \frac{\sqrt{|N'(\tau)|}}{N(\tau)} = 0. \quad (10)$$

A simple and monotone parameterization satisfying this property is the polynomial mapping

$$N(\tau) = \tau^{-2}, \quad \tau > 0. \quad (11)$$

This choice guarantees both the divergence of $N(\tau)$ as $\tau \rightarrow 0$ and a monotonically vanishing diffusion coefficient.

For the parameterization in Eq. (11) we have

$$\frac{\sqrt{|N'(\tau)|}}{N(\tau)} = \frac{\sqrt{2} \tau^{-3/2}}{\tau^{-2}} = \sqrt{2\tau}. \quad (12)$$

Substituting into Eq. (53) yields the explicit Monte Carlo SDE (MC-SDE):

$$dY(\tau) = \frac{2(Y(\tau) - \mu)}{\tau} d\tau + \sigma \sqrt{2\tau} dW_\tau. \quad (13)$$

Interpretation and discussion. Eq. (13) satisfies the desired monotone noise schedule: the diffusion amplitude $b(\tau) = \sigma \sqrt{2} \tau^{1/2}$ is strictly increasing with τ (for $\tau > 0$) and thus strictly decreasing as $\tau \rightarrow 0$, with $\lim_{\tau \rightarrow 0} b(\tau) = 0$. The drift term is $\frac{2}{\tau}(Y - \mu)$, which enforces convergence toward the mean at a rate proportional to $1/\tau$.

This makes sense with common observation. $\tau \rightarrow 0^+$ indicates $N \rightarrow \infty$, with more sampling counts, less noise, closer to real value. With Eq. (13), we have an exact math modelling to map Monte Carlo Sampling as a diffusion denoising process. More interesting discussion among Eq. (53), Eq. (11), and Eq. (13) including choice of $N(\tau)$, connection with Eq. (9), and further understanding can be found in our supplementary. Therefore, a more intelligent approach—such as a parameterized fitting function or a lightweight network—could be deployed in subsequent work to learn an adaptive mapping, thereby yielding more accurate and robust solutions.

3.2. Path Tracing in MC-SDE

We instantiate the MC-SDE for path tracing while enforcing a common noise source. Concretely, we use **uniform hemisphere sampling** for *both* diffuse and specular directions and reuse the *same* random sample per path. Under these conditions the stochastic fluctuations of both components share a common origin, and finite second moments ensure the multivariate CLT applies.

A standard render equation is often written as

$$\begin{aligned} L_o(\mathbf{p}, \boldsymbol{\omega}_o) &= \int_{\Omega} f_r(\mathbf{p}, \boldsymbol{\omega}_o, \boldsymbol{\omega}_i) L_i(\mathbf{p}, \boldsymbol{\omega}_i) (\mathbf{n} \cdot \boldsymbol{\omega}_i) d\boldsymbol{\omega}_i \\ &= \int_{\Omega} \left(k_d \frac{c}{\pi} + \frac{D \cdot F \cdot G}{4(\boldsymbol{\omega}_o \cdot \mathbf{n})(\boldsymbol{\omega}_i \cdot \mathbf{n})} \right) L_i(\mathbf{p}, \boldsymbol{\omega}_i) (\mathbf{n} \cdot \boldsymbol{\omega}_i) d\boldsymbol{\omega}_i. \end{aligned} \quad (14)$$

The integral over the hemisphere Ω includes the bidirectional reflectance distribution function (BRDF) [3, 7]

$f_r(\mathbf{p}, \boldsymbol{\omega}_o, \boldsymbol{\omega}_i)$, the incoming radiance $L_i(\mathbf{p}, \boldsymbol{\omega}_i)$, and the cosine factor $\mathbf{n} \cdot \boldsymbol{\omega}_i$, which is the cosine of the angle between the surface normal \mathbf{n} and the incoming direction $\boldsymbol{\omega}_i$, at sampling point \mathbf{p} . We use the Cook-Torrance model [7] as example, c is the albedo, and D , F , and G are the normal distribution function, Fresnel equation, and geometry function, respectively. The diffuse coefficient k_d is calculated as $(1 - k_s) \times m$, where k_s is equal to F , and m is the input material parameter metallic representing the metallic of the material.

Upon this, we can separate the diffuse $F_k^d = \frac{ck_d}{\pi} L_i(\mathbf{p}, \boldsymbol{\omega}_k)(\mathbf{n} \cdot \boldsymbol{\omega}_k)\boldsymbol{\omega}_k / \mathcal{P}(\boldsymbol{\omega}_k)$ and specular $F_k^s = \frac{D \cdot F \cdot G}{4(\boldsymbol{\omega}_o \cdot \mathbf{n})(\boldsymbol{\omega}_i \cdot \mathbf{n})} L_i(\mathbf{p}, \boldsymbol{\omega}_k)(\mathbf{n} \cdot \boldsymbol{\omega}_k)\boldsymbol{\omega}_k / \mathcal{P}(\boldsymbol{\omega}_k)$ components. Each sampled path contributes camera-bound radiance

$$F_S = F_k^s + F_k^d, \quad (15)$$

and the pixel estimator

$$X_N = \frac{1}{N} \sum_{k=1}^N F_S^{(k)} = X_N^d + X_N^s. \quad (16)$$

Assume the per-sample vector (F_k^s, F_k^d) has

$$\begin{aligned} \mu_d &= \mathbb{E}[F_k^d], & \mu_s &= \mathbb{E}[F_k^s], \\ \Sigma &= \text{Cov}[(F_k^s, F_k^d)^\top] = \begin{pmatrix} \sigma_d^2 & \sigma_{ds} \\ \sigma_{ds} & \sigma_s^2 \end{pmatrix}. \end{aligned} \quad (17)$$

Let $Y(\tau) = (Y_d(\tau), Y_s(\tau))^\top$ denote the continuous-time interpolation.

Vector MC-SDE with correlated noise. Under Eq. (11), the component process satisfies

$$dY(\tau) = \frac{2(Y(\tau) - \mu)}{\tau} d\tau + \sqrt{2\tau} \Sigma^{1/2} dB_\tau, \quad (18)$$

where $\mu = (\mu_d, \mu_s)^\top$, B_τ is a 2D standard Wiener process, and $\Sigma^{1/2}$ is any PSD factor with $\Sigma^{1/2}(\Sigma^{1/2})^\top = \Sigma$ (e.g., Cholesky). Thus the increment covariance is $2\tau \Sigma d\tau$. The scalar total $Y_{\text{tot}}(\tau) = Y_d(\tau) + Y_s(\tau)$ obeys

$$dY_{\text{tot}}(\tau) = \frac{2(Y_{\text{tot}}(\tau) - \mu_d - \mu_s)}{\tau} d\tau + \sigma_{\text{tot}} \sqrt{2\tau} dW_\tau, \quad (19)$$

with

$$\sigma_{\text{tot}}^2 = \text{Var}(F_k^s + F_k^d) = \sigma_d^2 + 2\sigma_{ds} + \sigma_s^2, \quad (20)$$

and a scalar Wiener process W_τ .

Equation (18) uses a single scalar Wiener for both components would implicitly assume $\text{rank}(\Sigma) = 1$. Under uniform hemisphere sampling the multivariate CLT ensures Gaussian fluctuations. In practical scene, $\sigma_s \gg \sigma_d$, therefore $\sigma_{\text{tot}} \approx \sigma_s$. Large specular variance simply makes σ_{tot} dominant in (19), matching the empirical observation that specular content dominates high-variance regimes.

3.3. MC-SDE Aligns with Diffusion Models

We start from the Monte Carlo SDE in Eq. (13), and show that it can be realized exactly as the reverse-time SDE of a simple variance-exploding (VE) forward process [34]. This provides a direct bridge between the Monte Carlo ‘‘variance time’’ τ and a diffusion model’s time t .

A virtual forward SDE. Consider the *forward* (fictitious) process $X(\tau)$ defined for $\tau \geq 0$ by

$$dX(\tau) = g(\tau) dW_\tau, \quad g(\tau) = \sigma\sqrt{2\tau}, \quad X(0) = \mu. \quad (21)$$

This is a drift-free VE-SDE whose marginal law is Gaussian with

$$\begin{aligned} \mathbb{E}[X(\tau)] &= \mu, \\ \text{Var}[X(\tau)] &= \int_0^\tau g(s)^2 ds = \int_0^\tau 2\sigma^2 s ds = \sigma^2 \tau^2. \end{aligned} \quad (22)$$

Hence $X(\tau) \sim \mathcal{N}(\mu, \sigma^2 \tau^2)$, which *exactly* matches the CLT variance of the Monte Carlo estimator under the reparameterization in Eq. (11).

For a general forward SDE $dX = f(X, \tau) d\tau + g(\tau) dW_\tau$ with marginal density p_τ , the reverse-time dynamics read

$$dY(\tau) = [f(Y, \tau) - g(\tau)^2 \nabla_y \log p_\tau(Y)] d\tau + g(\tau) d\bar{W}_\tau, \quad (23)$$

where \bar{W}_τ is a standard Wiener process in reverse time. Applying (23) to the VE forward process (21) with $f \equiv 0$ and $p_\tau = \mathcal{N}(\mu, \sigma^2 \tau^2)$ gives

$$\nabla_y \log p_\tau(y) = -\frac{y - \mu}{\sigma^2 \tau^2}, \quad g(\tau)^2 = 2\sigma^2 \tau,$$

and therefore

$$dY(\tau) = \frac{2(Y(\tau) - \mu)}{\tau} d\tau + \sigma\sqrt{2\tau} d\bar{W}_\tau, \quad (24)$$

which coincides with the MC-SDE (13). Thus, the MC-SDE is *precisely* the reverse SDE of the clean-start VE forward process (21). Decreasing $\tau \downarrow 0$ corresponds to denoising toward $X(0) = \mu$, while increasing τ adds Monte Carlo noise with variance $\sigma^2 \tau^2$.

Noise ordering between two processes. To compare Monte Carlo noise with diffusion noise, we place both processes on a shared, dimensionless *effective-noise* axis.

For a VP/DDPM-type forward process $x_t = \bar{\alpha}(t) x_0 + \sigma_{\text{VP}}(t) \varepsilon$, the per-dimension SNR and its log form are

$$\text{SNR}_{\text{VP}}(t) = \frac{\bar{\alpha}(t)^2}{\sigma_{\text{VP}}(t)^2},$$

$$\lambda_{\text{diff}}(t) := \log \text{SNR}_{\text{VP}}(t) = \log \bar{\alpha}(t)^2 - \log \sigma_{\text{VP}}(t)^2. \quad (25)$$

In our MC parameterization $Y(\tau) = \mu + \sigma\tau\varepsilon$, we analogously define

$$\begin{aligned} \text{SNR}_{\text{MC}}(\tau) &:= \frac{\kappa}{\sigma^2\tau^2}, \\ \lambda_{\text{MC}}(\tau) &:= \log \text{SNR}_{\text{MC}}(\tau) = \log \kappa - \log \sigma^2 - 2 \log \tau, \end{aligned} \quad (26)$$

where κ is a fixed reference signal power. We align the two processes by matching log-SNRs at the same level, $\lambda_{\text{diff}}(t) = \lambda_{\text{MC}}(\tau)$, which yields the mapper $t^*(\tau)$

$$t^*(\tau) = \lambda_{\text{diff}}^{-1}(-2 \log \tau + A), \quad (27)$$

where $A := \log \kappa - \log \sigma^2$ is a constant. Since $\lambda_{\text{diff}}(t)$ and $\lambda_{\text{MC}}(\tau)$ are both continuous and monotone along their denoising trajectories, Eq. (27) induces a unique, strictly monotone reparameterization $\tau(t)$. In practice, our $\tau \rightarrow t$ mapping simply discretizes this relation from the training $\bar{\alpha}$ schedule. Combined with $\tau = N^{-1/2}$, this yields a one-line mapping from sample count to model timestep. With this mapper, path traced images at arbitrary spp can be effectively integrated into diffusion models for editing, control, and denoising.

Specular component dominates. With the log-SNR alignment in Eq. (27), diffusion time t and MC variance-time τ lie on the same effective-noise axis. Define the recoverable bandwidth in diffusion and Monte-Carlo by the usual power-law model $S_{x_0}(f) \asymp |f|^{-p}$:

$$\begin{aligned} \eta_{\text{diff}}(t) &:= \frac{\sigma_{\text{VP}}(t)^2}{\bar{\alpha}(t)^2}, & f_c^{\text{diff}}(t) &\propto \eta_{\text{diff}}(t)^{-1/p}, \\ \eta_{\text{MC}}(\tau) &:= \sigma^2\tau^2, & f_c^{\text{MC}}(\tau) &\propto \eta_{\text{MC}}(\tau)^{-1/p}. \end{aligned} \quad (28)$$

Both f_c^{diff} and f_c^{MC} are monotone in their effective noise, so higher frequencies stabilize only at lower noise levels in either process. Let $f_s > f_d > 0$ denote representative frequencies for specular- and diffuse-dominated content, and define the diffusion stabilization time

$$t_R^\dagger := \inf\{t : f_c^{\text{diff}}(t) \geq f_R\}, \quad R \in \{\text{spec}, \text{diff}\}. \quad (29)$$

On the Monte Carlo side, we measure the accuracy scale for a relative threshold $\varepsilon > 0$ by

$$\tau_R^*(\varepsilon) := \sup\{\tau \geq 0 : \mathbb{E}(Y_R(\tau) - \mu_R)^2 \leq \varepsilon^2 \mu_R^2\} = \frac{\varepsilon |\mu_R|}{\sigma_R}, \quad (30)$$

where $Y_R(\tau) = \mu_R + \sigma_R\tau\varepsilon$ is the MC-SDE for component R . Equivalently, in terms of the sample count $N = \tau^{-2}$, the minimum number of samples required to reach the same relative accuracy satisfies

$$N_R^*(\varepsilon) := (\tau_R^*(\varepsilon))^{-2} \propto \frac{\sigma_R^2}{\varepsilon^2 \mu_R^2}. \quad (31)$$

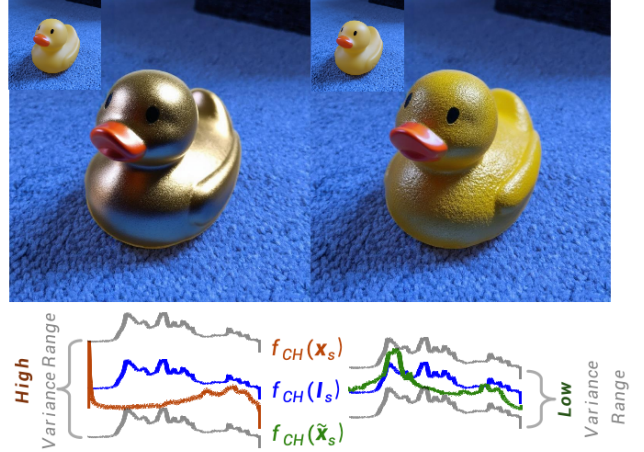


Figure 3. Effect of stage order on appearance and color statistics. Top-left inset: reference render I_S . We edit the reference image into to different materials, a specular one \mathbf{x}_s (left) and a diffuse one $\tilde{\mathbf{x}}_s$ (right). The bottom row plots the normalized color histogram $f_{CH}(\cdot)$ (RGB aggregated). Colors: blue = $f_{CH}(I_S)$, orange = $f_{CH}(\mathbf{x}_s)$, green = $f_{CH}(\tilde{\mathbf{x}}_s)$. Allocating a larger denoising range to the high-variance specular stage (left) produces metallic highlights/shadows and a sharper, heavier-tailed histogram; reversing the order compresses that range (right), yielding a smoother, low-contrast histogram. The gray band marks intensity zones where our MC-SDE prior predicts higher \rightarrow lower variance.

Since Sec. 3.2 gives $\sigma_{\text{spec}} \gg \sigma_{\text{diff}}$ in typical PBR scenes, under the monotone log-SNR alignment $\lambda_{\text{diff}}(t) = \lambda_{\text{MC}}(\tau)$ in Eq. (27), we obtain this ordering

$$N_{\text{spec}}^*(\varepsilon) \gg N_{\text{diff}}^*(\varepsilon) \Rightarrow t_{\text{spec}}^\dagger \geq t_{\text{diff}}^\dagger, \quad (32)$$

Eq. (32) indicates that specular content stabilizes strictly later along the diffusion trajectory, just as it converges later under Monte Carlo sampling. Intuitively, early diffusion steps correspond to low-spp, specular-noise-dominated regimes, and late steps to high-spp, diffuse-limited regimes. Fig. 3 illustrates this behavior with histograms of specular-like versus diffuse-like images: specular-evolved images exhibit a pronounced bias in color distribution and dynamic range, in contrast to more diffuse-like images. This specular dominance along the effective-noise axis allows us to control material components in the diffusion generation process in a principled way.

4. Experiments

The above derivation consequently unveils numerous promising avenues for further exploration and application. The first subsection, introduces a method to align the noise in low-sample-count (low spp) path tracing with the canonical noise distribution utilized in diffusion models.

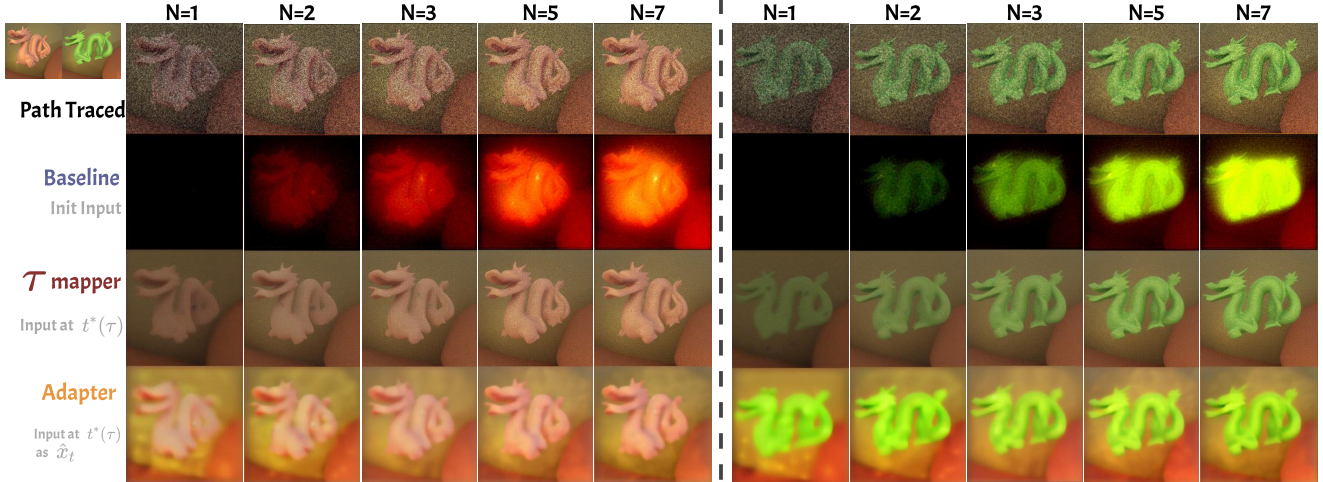


Figure 4. Diffusion Model takes over noisy path traced images. Top left is the path traced high spp images, as the ground truth. N is the sample count of the path traced image in its column. The first row indicates the input into the diffusion model. For the second row, we initialize the baseline latent noise with the corresponding sample count image. Regardless of the specific sample counts per image, we then subject it to a complete denoising process. For the third row, we use the $t^*(\tau)$ mapper to inject the image with its sample count N mapped to $t^*(\frac{1}{\sqrt{N}})$. And for the fourth row, we use an extra adapter to transform the noise distribution from Monte Carlo domain to diffusion domain, in the latent space. To summary up, our method of row 3 and 4 can make diffusion model understand the path traced noisy images. Directly mapping τ to t brings better shape restore, while an extra adapter can make diffusion model generate better color in diffusion’s noise space. All the guidance scale is set to 1.0 to test the generation result apart from prompt affects.

This alignment enables a pre-trained diffusion-based generative model to effectively process low-spp path-traced images and generate a clean output. In the second subsection, we introduce a method that leverages the distinct behavioral characteristics of specular and diffuse components at different stages of the denoising process to achieve fine-grained control over material appearance.

4.1. Diffusion takes over noisy path tracing images

A pre-trained diffusion model is, by nature, a generative model learned from 2D image data. Its capability to produce a desired image is solely contingent upon whether its training data encompasses the corresponding distribution. Yet, the characteristic noise and image distribution produced by path tracing fundamentally deviates from the training data distribution of the pre-trained diffusion model. Therefore, it is almost impossible to bypass the path tracing noise distribution training of a diffusion model and expect model to generate results that are perfectly consistent with path tracing ground truth, particularly given the multitude of inherent 3D constraints present in the path tracing process. Nevertheless, our approach substantially enhances the ability of pre-trained diffusion models to denoise low-spp path-traced images, leading to a marked improvement in output quality.

We can transform a low sample per pixel (spp) path traced image into diffusion model, leveraging Eq. (27). The visualization result is shown in figure 4, and the quantitative

comparison is on table 1. We sample 5 standard evaluation rendered scenes to conduct this experiment. And a training dataset with 30 scenes each including 14 different sample counts is built, to train our simple adapter.

In practical, we fix A in Eq. (27) from a target range $[N_{\min}, N_{\max}]$ by anchoring the noisiest point $\tau_{\max} = N_{\min}^{-1/2}$ and the cleanest point $\tau_{\min} = N_{\max}^{-1/2}$, then take A by calculating their average. After this, the discrete mapping is $t^*(\tau) = \arg \min_t |\lambda_{\text{diff}}(t) - (A - 2 \log \tau)|$. The result is shown in the **third row** in Fig. 4. Compared with the baseline, this method can map the low spp images into the fittest step, generate images with the correct shape and structure, while the baseline in the second row misunderstanding the inputs.

With the $t^*(\tau)$ mapper, we can match the noisy low spp path traced image into correct diffusion step. But as the information of the noisy input is too few and doesn’t cover the diffusion’s original noise distribution, the generated images have a low energy and appear dark. To bridge this gap, an exactly lightweight time-conditioned adapter is trained, to make the original noisy path traced image x_τ converted to \hat{x}_t following the diffusion’s noise distribution. The adapter predicts $\hat{x}_t = G_\theta(z_{\text{low}}, \phi(t))$. The loss emphasizes distribution alignment with four concise terms, (i) Maximum Mean Discrepancy; (ii) Moment Matching (mean/variance);(iii) Fourier Magnitude Matching. At inference we compute $(\tau, t^*(\tau))$, initialize with \hat{x}_t , and run deterministic DDIM to $t=0$, as shown in the fourth row in

Table 1. Quantitative Metrics of diffusion taking over in different methods. We compare these images with the high sample counts path traced images as the ground truth.

Methods	PSNR(\uparrow)	SSIM(\uparrow)	LPIPS(\downarrow)
low spp traced image	16.78	0.14	0.95
Baseline	11.24	0.23	0.78
τ Mapper	19.31	0.20	0.75
τ Mapper + adapter	20.72	0.71	0.37

Fig. 4. Compared with the third col, the adapter results have better color range and ground truth restore.

Table 1 shows that our τ Mapper in row 3 can out perform baseline in row 2 a lot and denoise the original image of row 1. Our adapter in row 4 can greatly improve the similarity to ground truth due to the distribution mapping. All the result is conducted on stable diffusion model *CompVis/stable-diffusion-v1-4*, if not otherwise indicated.

4.2. Material tuning based on noise stage

From Eq. (32) we have a key conclusion that the diffusion denoising process and path tracing process inherently share similar spectral characteristics. Specifically, under high noise levels, pixel values exhibit stronger dynamics, which preferentially facilitates the development of high-frequency features such as specular highlights. Consequently, we develop a simple but useful framework that enables fine-grained material editing by extending a foundational image editing method [33]. We keep the material-related text prompt fixed and then modulate the attention weights corresponding to the spatial locations of high-frequency tokens in the cross-attention map. This modulation is applied using a coefficient that is inversely correlated with the denoising timestep. As a result, this design enhances the influence of high-frequency features during the early stages of denoising and allows it to gradually fade out in later stages.

In detail, we set two material parameters, $r, m \in (0, 1)$, corresponding to the parameter in PBR. At timestep t , we will set the corresponding parameter token $A[index_{mat}]$ to a designed $Scaler_{Mat}$ on the attention map according to the material condition $Con_{Mat} \in (Con_m, Con_r)$, where $Con_m = \frac{T-t}{T} < m, Con_r = \frac{T-t}{T} > m$. If met condition Con_{Mat} , we set $A[index_{mat}]$ as $Scaler_{Mat}$; else just as zero. Further implementation details and comprehensive analysis of the material tuning framework are provided in the supplementary material.

Fine-grained Material Tuning. As shown in Figure 5, we present the continuity and diversity of material editing achieved by our simple framework, as m increases, the metallic visual concept grows obvious, the same as r .

Specular in noisy stage. We also verify the effectiveness of controlling the strength of the specular component

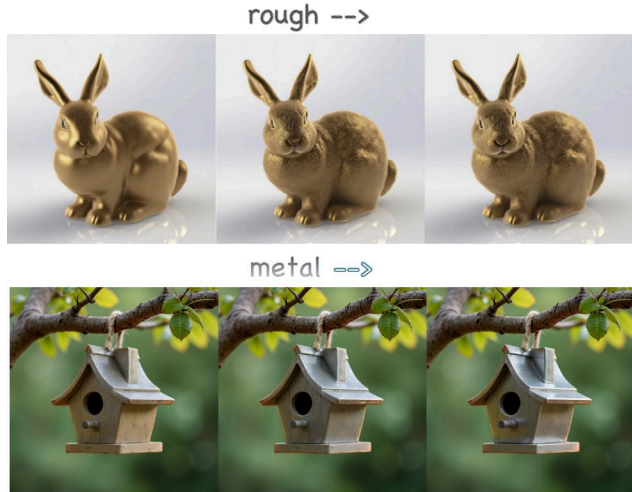


Figure 5. a simple framework for fine-grained material tuning. The first row presents growing degree of roughness r from left to right. Second row presents growing degree of metallic m , still from left to right. We use a easy trick to map the PBR parameter into diffusion model’s text space.



Figure 6. Result of reversed Con_{Mat} . $m = 0.5, r = 0.5$. Left: original image. Middle: our normal method result. Right: Reversed result. It could be found that the reversed result has lower respond and intention to be a metallic material specular part), even with the same parameter.

during the early stages of the denoising process, according to Eq. (32). So we design this process reversed, which strengthen the diffuse part in early denoising stage and specular part in later stage. In practical, we negate the Con_{Mat} . And the result is shown on Fig. 6. It is clearly observed that, under the same parameter conditions, when the condition is reversed, the specular components of the object significantly decrease. This precisely demonstrates the necessity of emphasizing the specular component during the early stages of denoising, when the noise level is higher. This precisely demonstrates the necessity of emphasizing the specular component during the early stages of denoising, when the noise level is higher.

5. Conclusion

In this paper, we investigated the relationship between PBR and diffusion models from the perspective of their analogous denoising processes. A physically grounded MC-SDE

is introduced to connect the denoising processes of diffusion models with Monte Carlo path tracing. This general SDE formulation is further analyzed from the perspective of noise variance, allowing the physical properties inherent to path tracing to be extended to existing diffusion models. Through experiments on both rendering and material editing tasks, we demonstrate that the proposed conclusions and methods enable physically grounded control over the diffusion-generated results.

References

- [1] Omri Avrahami, Dani Lischinski, and Ohad Fried. Blended diffusion for text-driven editing of natural images. In *CVPR*, pages 18208–18218, 2022. [2](#)
- [2] Tim Brooks, Aleksander Holynski, and Alexei A Efros. Instructpix2pix: Learning to follow image editing instructions. In *CVPR*, pages 18392–18402, 2023. [2](#)
- [3] Brent Burley and Walt Disney Animation Studios. Physically-based shading at disney. In *Acm Siggraph*, pages 1–7. vol. 2012, 2012. [4](#)
- [4] Mingdeng Cao, Xintao Wang, Zhongang Qi, Ying Shan, Xiaohu Qie, and Yinqiang Zheng. Masactrl: Tuning-free mutual self-attention control for consistent image synthesis and editing. *arXiv preprint arXiv:2304.08465*, 2023. [2](#)
- [5] Rui Chen, Yongwei Chen, Ningxin Jiao, and Kui Jia. Fantasia3d: Disentangling geometry and appearance for high-quality text-to-3d content creation. In *ICCV*, 2023. [2](#)
- [6] Yuren Cong, Martin Renqiang Min, Li Erran Li, Bodo Rosenhahn, and Michael Ying Yang. Attribute-centric compositional text-to-image generation. *arXiv preprint arXiv:2301.01413*, 2023. [2](#)
- [7] R. L. Cook and K. E. Torrance. A reflectance model for computer graphics. *ACM Trans. Graph.*, 1(1):7–24, 1982. [1](#), [4](#), [5](#)
- [8] Songwei Ge, Taesung Park, Jun-Yan Zhu, and Jia-Bin Huang. Expressive text-to-image generation with rich text. In *CVPR*, pages 7545–7556, 2023. [2](#)
- [9] Amir Hertz, Ron Mokady, Jay Tenenbaum, Kfir Aberman, Yael Pritch, and Daniel Cohen-Or. Prompt-to-prompt image editing with cross attention control. *arXiv preprint arXiv:2208.01626*, 2022. [2](#)
- [10] Jonathan Ho and Tim Salimans. Classifier-free diffusion guidance. In *NeurIPS*, 2021. [2](#)
- [11] Jonathan Ho, Ajay Jain, and Pieter Abbeel. Denoising diffusion probabilistic models. *Advances in neural information processing systems*, 33:6840–6851, 2020. [2](#)
- [12] Haian Jin, Yuan Li, Fujun Luan, Yuanbo Xiangli, Sai Bi, Kai Zhang, Zexiang Xu, Jin Sun, and Noah Snavely. Neural gaffer: Relighting any object via diffusion. In *Advances in Neural Information Processing Systems*, 2024. [2](#)
- [13] James T. Kajiya. The rendering equation. In *Proceedings of the 13th Annual Conference on Computer Graphics and Interactive Techniques*, page 143–150, New York, NY, USA, 1986. Association for Computing Machinery. [1](#)
- [14] Tero Karras, Miika Aittala, Timo Aila, and Samuli Laine. Elucidating the design space of diffusion-based generative models. In *NeurIPS*, 2022. [2](#)
- [15] Bahjat Kawar, Shiran Zada, Oran Lang, Omer Tov, Huiwen Chang, Tali Dekel, Inbar Mosseri, and Michal Irani. Imagic: Text-based real image editing with diffusion models. In *CVPR*, pages 6007–6017, 2023. [2](#)
- [16] Gwanghyun Kim, Taesung Kwon, and Jong Chul Ye. Diffusionclip: Text-guided diffusion models for robust image manipulation. In *CVPR*, pages 2426–2435, 2022. [2](#)
- [17] Peter Kocsis, Vincent Sitzmann, and Matthias Nießner. Intrinsic image diffusion for single-view material estimation. *arXiv preprint arXiv:2312.12274*, 2023. [2](#)
- [18] Ruofan Liang, Zan Gojic, Huan Ling, Jacob Munkberg, Jon Hasselgren, Zhi-Hao Lin, Jun Gao, Alexander Keller, Nandita Vijaykumar, Sanja Fidler, and Zian Wang. Diffusion-renderer: Neural inverse and forward rendering with video diffusion models. *arXiv preprint arXiv: 2501.18590*, 2025. [2](#)
- [19] Ruoshi Liu, Rundi Wu, Basile Van Hoorick, Pavel Tokmakov, Sergey Zakharov, and Carl Vondrick. Zero-1-to-3: Zero-shot one image to 3d object. In *ICCV*, pages 9298–9309, 2023. [2](#)
- [20] Xihui Liu, Zhe Lin, Jianming Zhang, Handong Zhao, Quan Tran, Xiaogang Wang, and Hongsheng Li. Open-edit: Open-domain image manipulation with open-vocabulary instructions. In *ECCV*, pages 89–106. Springer, 2020. [2](#)
- [21] Jian Ma, Junhao Liang, Chen Chen, and Haonan Lu. Subject-diffusion: open domain personalized text-to-image generation without test-time fine-tuning. *arXiv preprint arXiv:2307.11410*, 2023. [2](#)
- [22] Chenlin Meng, Yutong He, Yang Song, Jiaming Song, Jiajun Wu, Jun-Yan Zhu, and Stefano Ermon. SDEdit: Guided image synthesis and editing with stochastic differential equations. In *ICLR*, 2022. [2](#)
- [23] Ron Mokady, Amir Hertz, Kfir Aberman, Yael Pritch, and Daniel Cohen-Or. Null-text inversion for editing real images using guided diffusion models. In *CVPR*, pages 6038–6047, 2023. [2](#)
- [24] Chong Mou, Xintao Wang, Liangbin Xie, Yanze Wu, Jian Zhang, Zhongang Qi, Ying Shan, and Xiaohu Qie. T2i-adapter: Learning adapters to dig out more controllable ability for text-to-image diffusion models. *arXiv preprint arXiv:2302.08453*, 2023. [2](#)
- [25] Alexander Quinn Nichol, Prafulla Dhariwal, Aditya Ramesh, Pranav Shyam, Pamela Mishkin, Bob McGrew, Ilya Sutskever, and Mark Chen. Glide: Towards photorealistic image generation and editing with text-guided diffusion models. In *ICML*, pages 16784–16804, 2022. [1](#), [2](#)
- [26] Aditya Ramesh, Prafulla Dhariwal, Alex Nichol, Casey Chu, and Mark Chen. Hierarchical text-conditional image generation with clip latents. *arXiv preprint arXiv:2204.06125*, 2022.
- [27] Robin Rombach, Andreas Blattmann, Dominik Lorenz, Patrick Esser, and Björn Ommer. High-resolution image synthesis with latent diffusion models. In *CVPR*, pages 10684–10695, 2022. [1](#), [2](#)
- [28] Nataniel Ruiz, Yuanzhen Li, Varun Jampani, Yael Pritch, Michael Rubinstein, and Kfir Aberman. Dreambooth: Fine tuning text-to-image diffusion models for subject-driven generation. In *CVPR*, pages 22500–22510, 2023. [2](#)

- [29] Nataniel Ruiz, Yuanzhen Li, Varun Jampani, Wei Wei, Tingbo Hou, Yael Pritch, Neal Wadhwa, Michael Rubinstein, and Kfir Aberman. Hyperdreambooth: Hypernetworks for fast personalization of text-to-image models. *arXiv preprint arXiv:2307.06949*, 2023. 2
- [30] Chitwan Saharia, William Chan, Saurabh Saxena, Lala Li, Jay Whang, Emily L Denton, Kamyar Ghasemipour, Raphael Gontijo Lopes, Burcu Karagol Ayan, Tim Salimans, et al. Photorealistic text-to-image diffusion models with deep language understanding. *NeurIPS*, 35:36479–36494, 2022. 1, 2
- [31] Sam Sartor and Pieter Peers. Matfusion: A generative diffusion model for svbrdf capture. In *SIGGRAPH Asia 2023 Conference Papers*, pages 1–10, 2023. 2
- [32] Prafull Sharma, Varun Jampani, Yuanzhen Li, Xuhui Jia, Dmitry Lagun, Fredo Durand, William T. Freeman, and Mark Matthews. Alchemist: Parametric control of material properties with diffusion models. *arXiv preprint arXiv:2312.02970*, 2023. 2
- [33] Chaehun Shin, Jooyoung Choi, Heeseung Kim, and Sungroh Yoon. Large-scale text-to-image model with inpainting is a zero-shot subject-driven image generator. 2024. 8
- [34] Yang Song, Jascha Sohl-Dickstein, Diederik P Kingma, Abhishek Kumar, Stefano Ermon, and Ben Poole. Score-based generative modeling through stochastic differential equations. In *ICLR*, 2021. 2, 4, 5
- [35] Stability AI. Stable diffusion v2.1, 2022. <https://huggingface.co/stabilityai/stable-diffusion-2-1>. 1
- [36] Narek Tumanyan, Michal Geyer, Shai Bagon, and Tali Dekel. Plug-and-play diffusion features for text-driven image-to-image translation. In *CVPR*, pages 1921–1930, 2023. 2
- [37] Giuseppe Vecchio, Rosalie Martin, Arthur Roullier, Adrien Kaiser, Romain Rouffet, Valentin Deschaintre, and Tamy Boubekeur. Controlmat: A controlled generative approach to material capture. *arXiv preprint arXiv:2309.01700*, 2023. 2
- [38] Andrey Voynov, Kfir Aberman, and Daniel Cohen-Or. Sketch-guided text-to-image diffusion models. In *ACM SIGGRAPH 2023 Conference Proceedings*, 2023. 2
- [39] Andrey Voynov, Qinghao Chu, Daniel Cohen-Or, and Kfir Aberman. P+: Extended textual conditioning in text-to-image generation. *arXiv preprint arXiv:2303.09522*, 2023. 2
- [40] Daniel Watson, William Chan, Ricardo Martin-Brualla, Jonathan Ho, Andrea Tagliasacchi, and Mohammad Norouzi. Novel view synthesis with diffusion models. *arXiv preprint arXiv:2210.04628*, 2022. 2
- [41] Jianfeng Xiang, Jiaolong Yang, Binbin Huang, and Xin Tong. 3d-aware image generation using 2d diffusion models. *arXiv preprint arXiv:2303.17905*, 2023. 2
- [42] Guangxuan Xiao, Tianwei Yin, William T. Freeman, Frédo Durand, and Song Han. Fastcomposer: Tuning-free multi-subject image generation with localized attention. *arXiv preprint arXiv:2305.10431*, 2023. 2
- [43] Xudong Xu, Zhaoyang Lyu, Xingang Pan, and Bo Dai. Mat-lab: Material-aware text-to-3d via latent brdf auto-encoder. *arXiv preprint arXiv:2308.09278*, 2023. 2
- [44] Hu Ye, Jun Zhang, Sibio Liu, Xiao Han, and Wei Yang. Ip-adapter: Text compatible image prompt adapter for text-to-image diffusion models. *arXiv preprint arXiv:2308.06721*, 2023. 2
- [45] Chong Zeng, Yue Dong, Pieter Peers, Youkang Kong, Hongzhi Wu, and Xin Tong. Dilightnet: Fine-grained lighting control for diffusion-based image generation. In *ACM SIGGRAPH 2024 Conference Papers*, 2024. 2
- [46] Xianfang Zeng, Xin Chen, Zhongqi Qi, Wen Liu, Zibo Zhao, Zhibin Wang, Bin Fu, Yong Liu, and Gang Yu. Paint3d: Paint anything 3d with lighting-less texture diffusion models. *arXiv preprint arXiv:2312.13913*, 2023. 2
- [47] Zheng Zeng, Valentin Deschaintre, Iliyan Georgiev, Yannick Hold-Geoffroy, Yiwei Hu, Fujun Luan, Ling-Qi Yan, and Miloš Hašan. Rgb \leftrightarrow x: Image decomposition and synthesis using material- and lighting-aware diffusion models. In *ACM SIGGRAPH 2024 Conference Papers*, New York, NY, USA, 2024. Association for Computing Machinery. 2
- [48] Longwen Zhang, Qiwei Qiu, Hongyang Lin, Qixuan Zhang, Cheng Shi, Wei Yang, Ye Shi, Sibe Yang, Lan Xu, and Jingyi Yu. Dreamface: Progressive generation of animatable 3d faces under text guidance. *ACM Trans. Graph.*, 42(4), 2023. 2
- [49] Lvmin Zhang, Anyi Rao, and Maneesh Agrawala. Adding conditional control to text-to-image diffusion models. In *CVPR*, pages 3836–3847, 2023. 2
- [50] Lvmin Zhang, Anyi Rao, and Maneesh Agrawala. Adding conditional control to text-to-image diffusion models, 2023. 1

Bridging Physically Based Rendering and Diffusion Models with Stochastic Differential Equation

Supplementary Material

6. Mathematical Explanation

6.1. Analysis of σ_s and σ_d

This section we will discuss why σ_s is often greater than σ_d .

First, we separate the last ray into camera $x_k^{[0]}$ out as follows:

$$\begin{aligned} \mathbf{x}_k &= \mathbf{x}_k^{[0]} \hat{L}_{i,k} = \frac{(k_d \frac{c}{\pi} + \frac{DFG}{4(\omega_o \cdot \mathbf{n})(\omega_{i,k} \cdot \mathbf{n})}) \mathbf{n} \cdot \omega_{i,k}}{\mathcal{P}(\omega_{i,k})} \hat{L}_{i,k} \\ &= \frac{k_d \frac{c}{\pi} \mathbf{n} \cdot \omega_{i,k}}{\mathcal{P}(\omega_{i,k})} \hat{L}_{i,k} + \frac{DFG}{4(\omega_o \cdot \mathbf{n})(\omega_{i,k} \cdot \mathbf{n})\mathcal{P}(\omega_{i,k})} \mathbf{n} \cdot \omega_{i,k} \hat{L}_{i,k} \\ &= x_{k,d} + x_{k,s}, \end{aligned}$$

$$\text{where } \mathbf{x}_k^{[0]} = \frac{(k_d \frac{c}{\pi} + \frac{DFG}{4(\omega_o \cdot \mathbf{n})(\omega_{i,k} \cdot \mathbf{n})}) \mathbf{n} \cdot \omega_{i,k}}{\mathcal{P}(\omega_{i,k})}. \quad (33)$$

Then we can calculate σ_s and σ_d :

$$\begin{aligned} \sigma_d^2 &= \mathbb{E}(x_{k,d}^2) - \mathbb{E}^2(x_{k,d}) \\ &= \int_{\Omega} \frac{(ck_d \frac{\mathbf{n} \cdot \omega_i}{\pi} \hat{L}(\omega_i))^2}{\mathcal{P}(\omega_i)} d\omega_i - (\int_{\Omega} ck_d \frac{\mathbf{n} \cdot \omega_i}{\pi} \hat{L}(\omega_i) d\omega_i)^2, \\ \sigma_s^2 &= \mathbb{E}(x_{k,s}^2) - \mathbb{E}^2(x_{k,s}) \\ &= \int_{\Omega} \frac{(\frac{DFG}{4(\omega_o \cdot \mathbf{n})(\omega_i \cdot \mathbf{n})} \omega_i \cdot \mathbf{n} \hat{L}(\omega_i))^2}{\mathcal{P}(\omega_i)} d\omega_i \\ &\quad - (\int_{\Omega} \frac{DFG}{4(\omega_o \cdot \mathbf{n})(\omega_i \cdot \mathbf{n})} \omega_i \cdot \mathbf{n} \hat{L}(\omega_i) d\omega_i)^2. \end{aligned} \quad (34)$$

To analyse the ratio of specular to diffuse, we first assume the incoming light can be separated from the integral. As same as the paper definition, the sampling probability function $\mathcal{P}(\omega_i)$ is uniform hemisphere sampling, with which we calculate the upper bound:

$$\begin{aligned} \sigma_d^2 < \hat{\sigma}_d^2 &= (1-m) \int_{\Omega} \frac{(c \frac{\mathbf{n} \cdot \omega_i}{\pi} \hat{L}(\omega_i))^2}{\mathcal{P}(\omega_i)} d\omega_i \\ &\quad - (1-m) (\int_{\Omega} c \frac{\mathbf{n} \cdot \omega_i}{\pi} \hat{L}(\omega_i) d\omega_i)^2 \\ &= (1-m) \frac{c^2 L_c^2}{3}, \end{aligned}$$

$$\sigma_s^2 = \frac{L_c^2}{(4 \cos \theta_o)^2} [2\pi \int_{\Omega} (DFG(\omega_i))^2 d\omega_i - (\int_{\Omega} DFG(\omega_i) d\omega_i)^2], \quad (35)$$

L_c is the separated incoming light. After this, we write out

the ratio:

$$\begin{aligned} \frac{\sigma_s^2}{\sigma_d^2} &> \frac{\sigma_s^2}{\hat{\sigma}_d^2} \\ &= \frac{3}{(1-m)(4c \cdot \cos \theta_o)^2} [2\pi \int_{\Omega} (DFG(\omega_i))^2 d\omega_i - (\int_{\Omega} DFG(\omega_i) d\omega_i)^2] \\ &= \frac{3}{(1-m)(4c \cdot \cos \theta_o)^2} [2\pi J - I^2], \end{aligned}$$

where $J = \int_{\Omega} (DFG(\omega_i))^2 d\omega_i$, $I = \int_{\Omega} DFG(\omega_i) d\omega_i$. (36)

As we need to compare the exactly ratio, we need make the D, F, G more clearly, as below:

$$\begin{aligned} DFG(\omega_i) &= \frac{4\alpha^2}{\pi[(\alpha^2 - 1)(\mathbf{n} \cdot \mathbf{h}) + 1]^2} \\ &\quad \cdot [F_0 + (1 - F_0)(1 - \mathbf{h} \cdot \omega_o)^5] \\ &\quad \cdot \frac{\cos \theta_i \cos \theta_o}{(\cos \theta_i (1 - k) + k)(\cos \theta_o (1 - k) + k)}, \end{aligned} \quad (37)$$

where $\mathbf{h} = \frac{\omega_i + \omega_o}{|\omega_i + \omega_o|}$, $\alpha = r$,
 $k = \frac{\alpha^2}{2}$ or $\frac{(\alpha + 1)^2}{8}$,
 $\cos \theta_i = \mathbf{n} \cdot \omega_i$, $\cos \theta_o = \mathbf{n} \cdot \omega_o$.

, r is roughness, m is metallic parameter in PBR rendering. The hatted $\hat{\sigma}_d$ is greater than σ_d since we let $k_d = 1 - m$ rather than real value $(1 - F_0)(1 - m)$.

Now we have all the values now, and we can analyse the value of Equation 36. The integral I is always a finite value considering the design of microfacet function and energy conservation. When we set $\alpha \rightarrow 0$, the function DFG will have this intention, considering the max value:

$$\begin{aligned} \alpha \rightarrow 0, DFG(\omega_i)|_{max} &\propto \frac{1}{\alpha^2}, DFG^2(\omega_i) \propto \frac{1}{\alpha^4}, \\ \int_{\Omega} (DFG(\omega_i))^2 d\omega_i &\propto DFG^2(\omega_i)|_{max} \cdot \Delta u \propto \frac{1}{\alpha^4} \cdot \alpha^2 \rightarrow \infty \end{aligned} \quad (38)$$

Δu here can be regarded as FWHM area, which is proportional to square of α . While J approaching infinity, I is finite, the ratio has:

$$\frac{\sigma_s^2}{\hat{\sigma}_d^2} = \infty - I \rightarrow \infty, \sigma_s \gg \sigma_d, \alpha \rightarrow 0. \quad (39)$$

It is easier to analyse the ratio when m goes to 1, as we have $(1 - m)$ in the denominator. The ratio will directly increase to infinity.

$$\frac{\sigma_s^2}{\hat{\sigma}_d^2} \propto \frac{1}{1 - m} \rightarrow \infty, \sigma_s \gg \sigma_d, m \rightarrow 1. \quad (40)$$

Thus, in typical rendering scenarios without complete diffuse dominance, a substantial disparity in variance is observed between specular and diffuse components, with specular variance markedly surpassing its diffuse counterpart.

6.2. Understanding of the Drift Term Behavior as $\tau \rightarrow 0$

For completeness, we clarify the behavior of the drift term in the Monte Carlo SDE

$$dY(\tau) = \frac{2(Y(\tau) - \mu)}{\tau} d\tau + \sigma_{\text{tot}} \sqrt{2\tau} dW_\tau, \quad (41)$$

corresponding to the choice

$$N(\tau) = \tau^{-2}, \quad \tau > 0, \quad (42)$$

introduced in the main paper.

CLT scaling under $N(\tau) = \tau^{-2}$. Recall the discrete Monte Carlo estimator

$$X_N = \frac{1}{N} \sum_{k=1}^N F_k, \quad \mathbb{E}[F_k] = \mu, \quad \text{Var}(F_k) = \sigma^2, \quad (43)$$

for i.i.d. samples $\{F_k\}$ with finite mean and variance. By the Central Limit Theorem, as $N \rightarrow \infty$ we have

$$X_N - \mu = \mathcal{O}_p(N^{-1/2}). \quad (44)$$

In our continuous parameterization, the process is defined by

$$Y(\tau) := X_{N(\tau)}, \quad N(\tau) = \tau^{-2}. \quad (45)$$

Substituting $N(\tau)$ into the CLT scaling yields

$$Y(\tau) - \mu = \mathcal{O}_p(N(\tau)^{-1/2}) = \mathcal{O}_p(\tau), \quad \tau \rightarrow 0^+. \quad (46)$$

Thus, as we approach the noise-free limit $\tau \rightarrow 0$, the empirical deviation from the mean contracts *linearly* in τ .

Drift coefficient and its apparent singularity. In Eq. (41), the drift coefficient is

$$b(Y(\tau), \tau) = \frac{2(Y(\tau) - \mu)}{\tau}. \quad (47)$$

Using the CLT-induced scaling $Y(\tau) - \mu = \mathcal{O}_p(\tau)$, we obtain

$$b(Y(\tau), \tau) = \frac{2\mathcal{O}_p(\tau)}{\tau} = \mathcal{O}_p(1), \quad \tau \rightarrow 0^+. \quad (48)$$

In other words, although b contains an explicit factor $1/\tau$, this is exactly compensated by the linear decay of $Y(\tau) - \mu$.

The drift coefficient remains of order one in probability and does *not* blow up as $\tau \rightarrow 0$.

Consequently, the infinitesimal drift increment in the SDE

$$b(Y(\tau), \tau) d\tau \quad (49)$$

is of order $\mathcal{O}_p(d\tau)$. Its time integral over any finite interval $[0, \tau_0]$ is therefore bounded in L^2 :

$$\int_0^{\tau_0} \frac{2(Y(\tau) - \mu)}{\tau} d\tau \text{ is finite and well-behaved.} \quad (50)$$

This is fully consistent with the discrete Monte Carlo estimator, which converges to μ at rate $N^{-1/2}$; our choice $N(\tau) = \tau^{-2}$ simply re-parameterizes this convergence so that it appears as a linear decay in the ‘‘variance time’’ τ .

Consistency with the diffusion term. For the same mapping $N(\tau) = \tau^{-2}$, the diffusion coefficient in Eq. (41) scales as

$$\sigma_{\text{tot}} \sqrt{2\tau}, \quad (51)$$

which vanishes as $\tau \rightarrow 0^+$. Hence, both drift and diffusion remain controlled in the limit: the process $Y(\tau)$ converges to the true expectation μ while the stochastic fluctuations are gradually switched off.

Interpretation. The term

$$\frac{2(Y(\tau) - \mu)}{\tau} \quad (52)$$

can be viewed as a *corrective gradient* that pulls the estimator toward μ . With the specific parameterization $N(\tau) = \tau^{-2}$, the CLT guarantees that $Y(\tau) - \mu$ decays proportionally to τ , so the seemingly singular factor $1/\tau$ merely expresses the fast convergence induced by increasing samples. Therefore, the MC-SDE in Eq. (41) is fully consistent with classical Monte Carlo behavior: it preserves unbiasedness, achieves variance reduction at the CLT rate, and remains well-behaved near $\tau = 0$ despite the apparent $1/\tau$ term in the drift.

6.3. Selection of $N(\tau)$

Recall the universal Monte Carlo SDE:

$$dY(\tau) = (\mu - Y(\tau)) \frac{N'(\tau)}{N(\tau)} d\tau + \sigma \frac{\sqrt{|N'(\tau)|}}{N(\tau)} dW_\tau. \quad (53)$$

One condition $\lim_{\tau \rightarrow 0} \frac{\sqrt{|N'(\tau)|}}{N(\tau)} = 0$ should be met to align with diffusion’s reverse SDE. It is readily observable that such a function of polynomial family $N(\tau) = \tau^{-p}$ ($p > 1$) straightforwardly satisfies the specified constraints. For details, please refer to the following.

Polynomial family $N(\tau) = \tau^{-p}$. Starting from the general Monte Carlo SDE in Eq. (53), we consider a polynomial family of mappings from the variance time τ to the effective sample count:

$$N(\tau) = \tau^{-p}, \quad p > 0, \tau > 0. \quad (54)$$

This choice ensures $N(\tau) \rightarrow \infty$ as $\tau \rightarrow 0^+$, i.e., smaller τ corresponds to more samples and lower Monte Carlo variance.

For Eq. (54), the derivative and its ratio to $N(\tau)$ are

$$\begin{aligned} N'(\tau) &= \frac{d}{d\tau} \tau^{-p} = -p\tau^{-p-1}, \\ \frac{N'(\tau)}{N(\tau)} &= \frac{-p\tau^{-p-1}}{\tau^{-p}} = -\frac{p}{\tau}. \end{aligned} \quad (55)$$

Substituting into the drift term of Eq. (53) gives

$$(\mu - Y(\tau)) \frac{N'(\tau)}{N(\tau)} = (\mu - Y(\tau)) \left(-\frac{p}{\tau}\right) = \frac{p}{\tau} (Y(\tau) - \mu), \quad (56)$$

so the negative sign is absorbed into $(Y(\tau) - \mu)$ and the drift still pulls the process toward the mean μ .

Similarly, the diffusion coefficient becomes

$$\frac{\sqrt{|N'(\tau)|}}{N(\tau)} = \frac{\sqrt{p\tau^{-p-1}}}{\tau^{-p}} = \sqrt{p}\tau^{\frac{p}{2}-\frac{1}{2}} = \sqrt{p}\tau^{\frac{p-1}{2}}. \quad (57)$$

Substituting these expressions into Eq. (53), we obtain the *polynomial Monte Carlo SDE*:

$$dY(\tau) = \frac{p}{\tau} (Y(\tau) - \mu) d\tau + \sigma \sqrt{p}\tau^{\frac{p-1}{2}} dW_\tau. \quad (58)$$

Behavior for different exponents p . The diffusion amplitude in Eq. (58) is

$$b(\tau) = \sigma \sqrt{p}\tau^{\frac{p-1}{2}}. \quad (59)$$

Its limit as $\tau \rightarrow 0^+$ is

$$\lim_{\tau \rightarrow 0^+} b(\tau) = \begin{cases} 0, & p > 1, \\ \sigma, & p = 1, \\ +\infty, & 0 < p < 1. \end{cases} \quad (60)$$

Therefore, any $p > 1$ yields a strictly decreasing noise level that vanishes as $\tau \rightarrow 0$, which matches the intuition that the estimator becomes noise-free in the infinite-sample limit and mimics the behavior of a diffusion reverse SDE with vanishing terminal noise. The case $p = 1$ corresponds to a constant noise amplitude near $\tau = 0$, while $0 < p < 1$ would make the noise explode as $\tau \rightarrow 0$, which is undesirable for a denoising process. It is worth noting that the formulation of this SDE remains mathematically rigorous

for any $p > 0$. However, to better align with the reverse SDE in diffusion modeling, selecting $p > 1$ is empirically preferred as it more effectively exploits the shared characteristics between the two processes of path tracing and diffusion denoising. As a special case, choosing $p = 2$ reduces Eq. (58) to

$$dY(\tau) = \frac{2}{\tau} (Y(\tau) - \mu) d\tau + \sigma\sqrt{2\tau} dW_\tau, \quad (61)$$

which is exactly the MC-SDE in main paper.

7. Experiments Details

This section we will introduce our extra experiments and more details. The first subsection presents the implementation details of our adapter training. Then more experiments are conducted and analyzed.

7.1. Adapter Training Details

We train a small distribution adapter G_θ that maps Monte Carlo (MC) low-SPP latents to diffusion-model latents at a matched noise level.

Inputs and targets. From the path-traced dataset we form pairs $(x_{\text{low}}(N), x_{\text{ref}})$, where $x_{\text{low}}(N)$ is rendered with SPP N and x_{ref} is the highest-SPP image in the same group. Both are resized to 512×512 and normalized to $[-1, 1]$, then encoded by the frozen Stable Diffusion VAE encoder \mathcal{E}_ϕ with scaling factor s :

$$z_{\text{low}} = s \mathcal{E}_\phi(x_{\text{low}}), \quad z_{\text{ref}} = s \mathcal{E}_\phi(x_{\text{ref}}). \quad (62)$$

For each SPP value N we define an MC ‘‘variance time’’ $\tau(N) = 1/\sqrt{\max(N, 1)}$ and map it to a diffusion timestep $t(N) \in \{0, \dots, T-1\}$ via a precomputed log-SNR curve $\{\lambda_t\}$ of a DDIM scheduler:

$$t(N) = \arg \min_t |\lambda_t - \lambda_{\text{target}}(\tau(N))|, \quad (63)$$

with $\lambda_{\text{target}}(\tau)$ chosen to match the range of $\{\lambda_t\}$ (details in the main text). Given z_{ref} and t , the diffusion-model latent at step t is

$$x_t^{\text{DM}} = \sqrt{\bar{\alpha}_t} z_{\text{ref}} + \sqrt{1 - \bar{\alpha}_t} \varepsilon, \quad \varepsilon \sim \mathcal{N}(0, I), \quad (64)$$

where $\bar{\alpha}_t$ is the cumulative product of DDIM alphas. The adapter output \hat{x}_t is trained to match the distribution of x_t^{DM} .

Adapter architecture. The adapter G_θ is a lightweight convolutional network with FiLM time conditioning. For each sample, we compute a sinusoidal time embedding $e_t \in \mathbb{R}^{d_t}$ from t , feed it to a small MLP to obtain per-channel

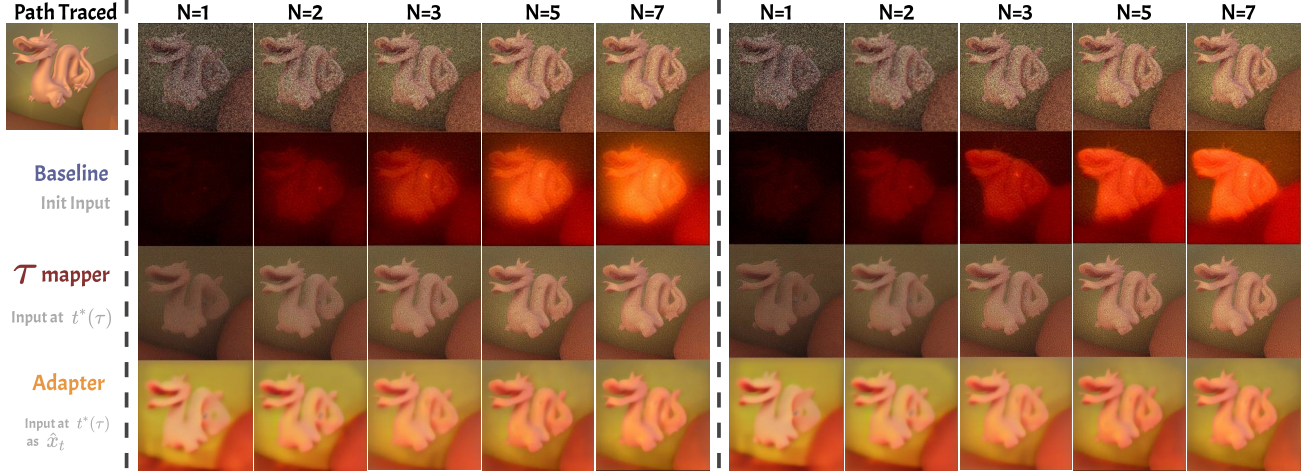


Figure 7. No prompt (left, cfg 1.0) vs prompt (right, cfg 7.5) results. The prompt is *A pink cartoon-style dragon in mid-flight, with open mouth and dorsal spikes, against a geometric background of greenish and brownish tones, in a smooth 3D fantasy theme* captioned by DeepSeek-R1. Our method generalizes effectively to out-of-distribution data from the test set, consistently preserving structural shapes and low-frequency details while maintaining robust performance.

scale and shift (γ, β) , and modulate an intermediate feature map:

$$\hat{x}_t = G_\theta(z_{\text{low}}, e_t). \quad (65)$$

Concretely, G_θ consists of:

- an input 3×3 convolution from 4 to H_{hid} channels,
- an MLP from e_t to $(\gamma, \beta) \in \mathbb{R}^{2H_{\text{hid}}}$,
- FiLM modulation $h \mapsto \gamma \odot h + \beta$,
- a mid 3×3 convolution in H_{hid} channels,
- a final 3×3 convolution projecting back to 4 channels,
- SiLU activations after convolutions.

The VAE and scheduler are frozen; only G_θ is optimized.

Distribution alignment losses. We align the distributions of \hat{x}_t and x_t^{DM} using a weighted combination of complementary losses.

(1) MMD loss. On spatially pooled features $\tilde{x}^{\text{MMD}} = P_{\text{mmd}}(\hat{x}_t)$ and $\tilde{y}^{\text{MMD}} = P_{\text{mmd}}(x_t^{\text{DM}})$, we apply a multi-scale RBF MMD:

$$\mathcal{L}_{\text{MMD}} = \sum_{\sigma \in \mathcal{S}} \text{MMD}_{k_\sigma}^2(\{\tilde{x}_i^{\text{MMD}}\}, \{\tilde{y}_i^{\text{MMD}}\}), \quad (66)$$

where \mathcal{S} is a small set of RBF bandwidths.

(2) Mean-variance matching. We match per-sample, per-channel spatial means and standard deviations:

$$\mathcal{L}_{\text{MV}} = \frac{1}{C} \sum_c \left\| \mu_c(\hat{x}_t) - \mu_c(x_t^{\text{DM}}) \right\|_2^2 + \left\| \sigma_c(\hat{x}_t) - \sigma_c(x_t^{\text{DM}}) \right\|_2^2. \quad (67)$$

(3) Spectral amplitude loss. On pooled features $\tilde{x}^{\text{spec}} = P_{\text{spec}}(\hat{x}_t)$ and $\tilde{y}^{\text{spec}} = P_{\text{spec}}(x_t^{\text{DM}})$, we match the magnitude of their 2D FFTs:

$$\mathcal{L}_{\text{spec}} = \left\| \left| \mathcal{F}(\tilde{x}^{\text{spec}}) \right| - \left| \mathcal{F}(\tilde{y}^{\text{spec}}) \right| \right\|_2^2. \quad (68)$$

(4) Content anchor. To preserve the low-frequency structure of the reference, we align a downsampled version of \hat{x}_t with $\sqrt{\alpha_t} z_{\text{ref}}$:

$$\mathcal{L}_{\text{anchor}} = \left\| P_{\text{anchor}}(\hat{x}_t) - P_{\text{anchor}}(\sqrt{\alpha_t} z_{\text{ref}}) \right\|_1. \quad (69)$$

(5) Range regularization. We prevent rare extreme activations in \hat{x}_t by encouraging it to stay within a channel-wise interval determined by the mean and standard deviation of x_t^{DM} . Let m_c, s_c be per-channel statistics of x_t^{DM} and k_σ a fixed multiplier. The loss penalizes squared deviations of \hat{x}_t outside $[m_c - k_\sigma s_c, m_c + k_\sigma s_c]$:

$$\mathcal{L}_{\text{range}} = \mathbb{E} \left[\left(\hat{x}_t - \text{clip}_{m \pm k_\sigma s}(\hat{x}_t) \right)^2 \right]. \quad (70)$$

(6) Low- t identity regularization. For timesteps below a threshold t_{thr} , we encourage the adapter to behave close to identity:

$$\mathcal{L}_{\text{id}} = \mathbb{E} \left[\left\| \hat{x}_t - z_{\text{low}} \right\|_2^2 \mathbb{1}_{t \leq t_{\text{thr}}} \right]. \quad (71)$$

Total objective and optimization. The final training loss is

$$\mathcal{L}_{\text{total}} = w_{\text{MMD}} \mathcal{L}_{\text{MMD}} + w_{\text{MV}} \mathcal{L}_{\text{MV}} + w_{\text{spec}} \mathcal{L}_{\text{spec}} + w_{\text{anchor}} \mathcal{L}_{\text{anchor}} + w_{\text{range}} \mathcal{L}_{\text{range}} + w_{\text{id}} \mathcal{L}_{\text{id}}. \quad (72)$$

We optimize G_θ with AdamW and a cosine learning-rate schedule with warmup. The VAE and diffusion scheduler are kept frozen; numerically sensitive operations (MMD, FFT, statistics) are evaluated in FP32 for stability, while the rest of the training loop may use mixed precision.

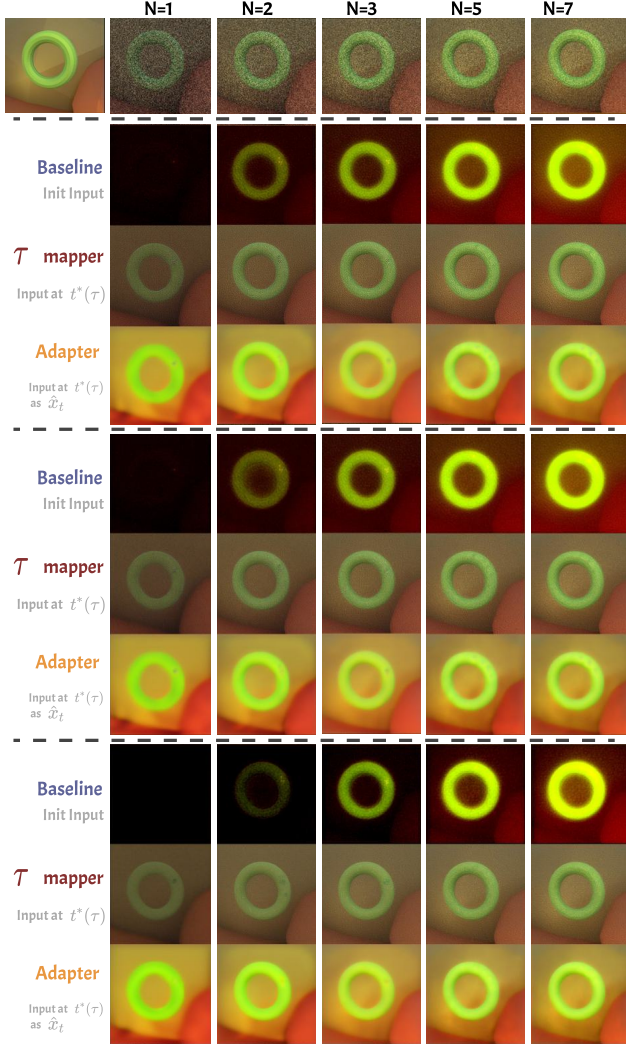


Figure 8. Quality comparison in different base models of our methods and adapter. Top, middle and bottom are Stable Diffusion version 1.4, 1.5 and 2.1 respectively.

7.2. Extra Experiments

Multi-baseline. We begin with a comparative evaluation of qualitative and quantitative results across different base models, including Stable Diffusion versions 1.4, 1.5, and 2.1. The quantitative results are presented in Table 2, qualitative results are shown in Figure 8. It can be observed that our raw method (τ mapper) requires no training and demonstrates effective adaptation across a range of models. Our adapter, while utilizing the VAE from Stable Diffusion 1.5, maintains full functional compatibility with other model architectures. This versatility stems from its theoretically-grounded design based on mathematical distribution alignment rather than specialized fitting to any specific model. The results further validate the general applicability of our theoretical framework.

Table 2. Quantitative comparison in different base models of our methods and adapter.

Methods	PSNR(\uparrow)	SSIM(\uparrow)	LPIPS(\downarrow)
low spp traced image	11.28	0.14	0.95
Baseline-sdv1-4	11.24	0.24	0.78
τ Mapper	19.33	0.21	0.75
τ Mapper + adapter	21.16	0.65	0.35
Baseline-sdv1-5	11.24	0.23	0.78
τ Mapper	19.31	0.20	0.75
τ Mapper + adapter	20.72	0.71	0.37
Baseline-sdv2-1	10.13	0.20	0.78
τ Mapper	22.34	0.28	0.64
τ Mapper + adapter	21.59	0.67	0.36

Prompt evaluation. We additionally evaluated the effect of prompt conditioning versus unconditional generation. As shown in Fig 7, our method yields consistently favorable results regardless of whether prompt conditioning is applied.

8. Limitations and Future Work

Selection of τ mapper. In the main paper, we use $t(N) = \arg \min_t |\lambda_{diff} - (A - 2 \log \tau(N))|$, and we use two N_{min}, N_{max} to calculate the average A . In practical, we choose $N_{min} = 0.001, N_{max} = 5000$. These two values are empirically derived. While they demonstrate broad applicability across most common scenarios, they are not theoretically optimal solutions and therefore cannot guarantee the best possible estimates under all conditions. Indeed, the parameter A may vary significantly across individual ray-traced images. Ideally, each low spp path-traced image should have an instance-specific mapper $t(N, x_N)$ that adapts to its unique characteristics X_N and the sample counts N . Therefore, a more intelligent approach—such as a parameterized fitting function or a lightweight network—could be deployed in subsequent work to learn an adaptive mapping, thereby yielding more accurate and robust solutions.

CLT conditions without importance sampling. Our derivation of the Monte Carlo SDE assumes a classical setting where samples are i.i.d. with finite variance and are drawn from a fixed underlying distribution, without explicitly modeling importance sampling, multiple importance sampling, or path-guided strategies. Under this assumption, the Central Limit Theorem provides a clean Gaussian approximation and leads to a simple drift-diffusion structure parameterized only by (μ, σ^2) and the sample count N . In practical rendering systems, however, importance weights, mixture weights, and correlations between paths may significantly distort the effective variance and even the

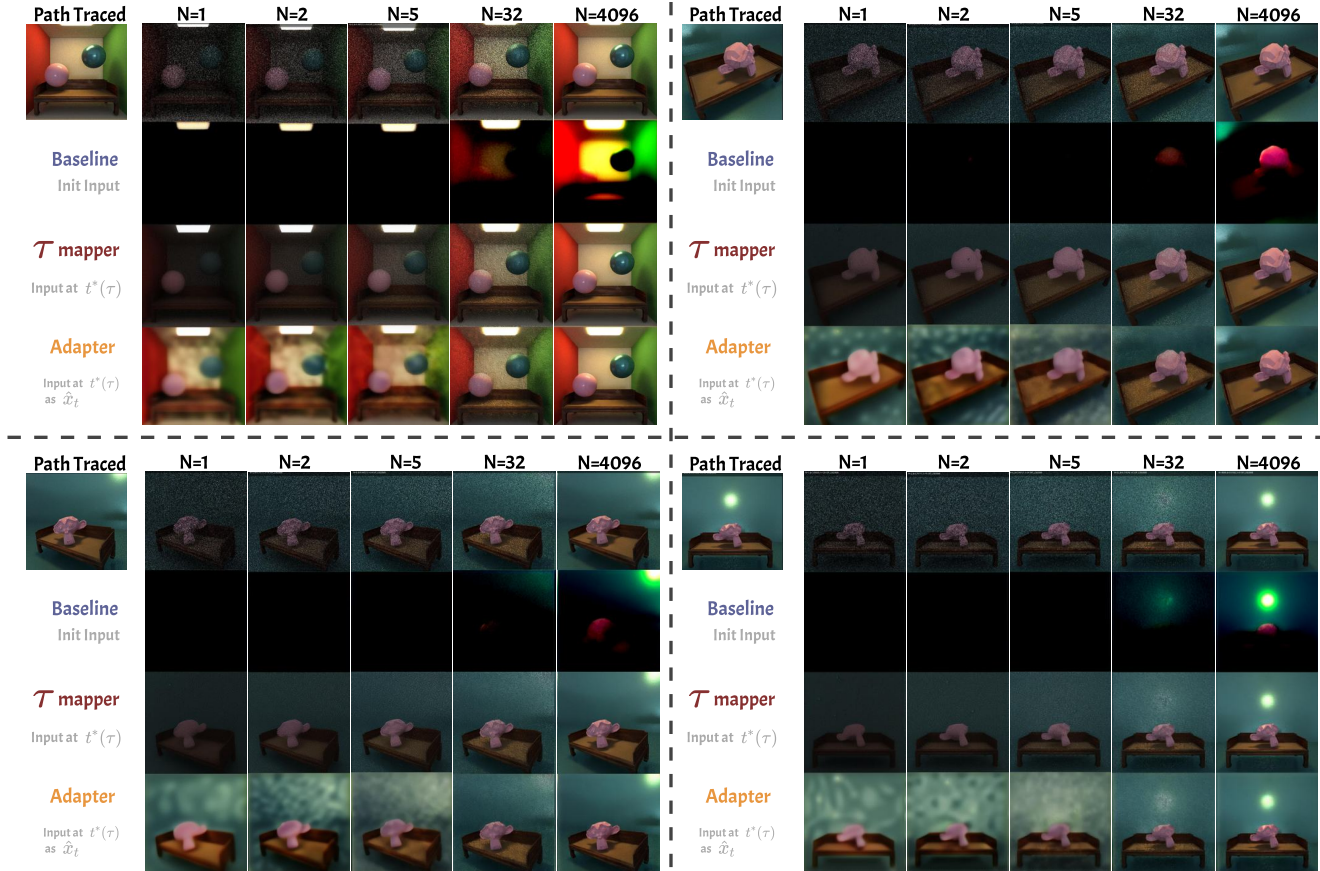


Figure 9. This figure depicts more complex scenarios, including sophisticated illumination environments and rendering results from multiple viewpoints. It is noteworthy that our adapter demonstrates strong generalization capability, successfully aligning the lighting color and distribution of unseen data and complex scenes with the target characteristics of the diffusion model.

tail behavior of the estimator, especially for complex transport effects such as caustics or participating media. Although CLT-type results still hold under broad conditions for importance-weighted estimators, the resulting SDE coefficients would depend intricately on the sampling scheme and scene configuration. A promising direction for future work is to extend the MC-SDE analysis to general importance sampling and multiple importance sampling, explicitly characterizing how different weighting strategies reshape the effective “variance time” τ , and to validate these extended models on production-grade path tracers with advanced guiding techniques.

Downstream work. In this paper, our experiments focus on a relatively constrained downstream task: mapping low-spp Monte Carlo renderings to the noise states of a pre-trained 2D diffusion model and edit the attention map to edit the material by the $t_{\text{spec}}^\dagger \geq t_{\text{diff}}^\dagger$. We do not yet explore more complex settings such as dynamic lighting, animated scenes, high-resolution film pro-

duction assets, or multi-view and 3D-consistent generation. Future work may extend the MC-SDE framework to broader downstream applications, including temporally coherent low-spp denoising, inverse rendering and relighting, view-consistent novel view synthesis, and 3D generative modeling of radiance fields or volumetric data. Incorporating richer rendering-side signals and geometry-aware conditioning into the adapter, or jointly training a diffusion model with MC-SDE-inspired objectives, could further tighten the connection between physically based rendering and generative modeling.